Laser shock peening enables 3D gradient metal structures: A case study on manufacturing self-armored hydrophobic surfaces

Abstract

Gradient heterostructures typically exhibit excellent mechanical properties. The traditional laser shock method can produce only 1D or 2D gradient structures along the thickness of a material. In this study, we propose a technique called 3D gradient laser shock peening without coating (3LSPwoC) for manufacturing 3D gradient metal structures. An excellent application of this method is the manufacture of multi-scale hydrophobic surfaces with integrated enhanced armor (IE-armor) in a flexible, large-scale and low-cost manner. Hydrophobic surfaces of metals are of great importance, but are typically mechanically fragile and degrade quickly, as the surface nanostructures tend to break under mechanical forces. Current approaches either expose the functional large-aspect-ratio nanostructures directly to external forces or have unbalanced strength-ductility synergy for dynamic loads, resulting in degradation of the properties. A self-armored hydrophobic surface structure was obtained by a combination of laser shock and low surface energy treatment. An IE-armor structure with a well-designed strength-ductility synergy was considered to protect the rich nano-hydrophobic structures. The arrayed micro-pits and abundant micro-nano structures in the pits realized a stable Cassie-Baxter state, resulting in a superhydrophobic surface. The alternating regular distribution of hard and sub-hard domains on the metal surface, together with the soft domain in the core, formed a 3D gradient structure, which achieved excellent synergistic plastic deformation and provided superior mechanical robustness. The 3D gradient metal structure manufactured using the 3LSPwoC process is expected to play a crucial role in highly reliable functional surfaces in aerospace, locomotive manufacturing, and ocean engineering.

Keywords: Laser shock; 3D gradient structure; Hydrophobic properties; Mechanical properties

1. Introduction

The hydrophobicity of a material's surface is of significant importance for realizing anti-icing, anti-fouling, self-cleaning and corrosion-prohibitive applications, and thus determines the service life of the material [1–3]. Researchers have used different process methods to effectively control the hydrophobic properties of metal surfaces by adjusting their microscopic morphology and chemical composition [4–7]. However, the main technical bottlenecks restricting large-scale applications of existing hydrophobic structuring methodologies are the fragility of the fabricated hydrophobic structures and the lack of flexibility in the processing technology for 3D surfaces with various compositions [8–10]. Under complex multi-physical external environmental loads, such as cyclic mechanical loading, chemical corrosion, and abrasion, the reliability of the hydrophobic structure is rapidly reduced. Thus, the performance in these situations is highly related to the defect evolution and mechanical properties of the surface and sub-surface.

A mechanically robust hydrophobic design based on microscale armor and nanoscale hydrophobic structures is introduced to alleviate the exclusiveness of mechanical robustness and water repellence. Deng et al. [11] suggested a microscale ceramic or bulk-deformed metal armor structure design to address this problem. Ceramic armor requires lithography and multiple other complicated processes, and has compatibility problems with the substrates. Metal armor fabrication requires high-pressure deformation of the bulk material, resulting in changes in part geometry and internal metallurgical structures, which is not acceptable in most cases. Therefore, for large-scale industrial applications, it is not yet feasible to fabricate such armors on targeted surfaces without degrading the integrity or geometric precision of the target, in addition to the economic and efficiency reasons.

Laser surface structuring is believed to be an enabling technology for hydrophobic surface fabrication [12–15]. Femtosecond laser direct ablation of the target material to generate various nanoscale features has drawn intense attention in the recent decades [16–18]. Guo et al. [19–21] reported the femtosecond laser treatment of metals to achieve hydrophobic, black, and water-repellent surfaces. However, femtosecond lasers have various delicate optics, making the process expensive and inefficient for large-scale applications. Pulsed laser shock imprinting can generate metallic surface structures with high precision and higher yield [22–25]. Ultra-smooth three-dimensional crystalline metal structures with sub-10 nm precision can be fabricated in atmospheric environments [26]. However, the substrates are restricted in terms of their thickness and the molds used are expensive to fabricate.

Direct laser ablation with long pulses (~ ns) can increase the efficiency, lower the fabrication cost and overcome the thickness restriction [27,28]. Various researchers [29–31] employed a high-energy nanosecond pulsed laser to texture the

surface of a material, and with the help of low-surface-energy reagents, a cross-scale micro-nano composite superhydrophobic surface structure could be obtained. However, the treated surfaces typically become brittle and unarmored, resulting in mechanical contact-induced fracture of the functional nanostructures, less energy absorption under dynamic loading, and fragile surface mechanical properties. To increase the overall mechanical properties of metal surfaces, Liu et al. [32] used a surface mechanical attrition treatment (SMAT) technique based on the shot peening process to introduce soft and hard domains on the surface of copper to balance the relationship between strength and ductility. This process also results in dense nanotwins that are typically ductile and strong. Shot peening improves the mechanical properties of the material, but the surface morphology cannot be effectively controlled. For the fabrication of durable hydrophobic surfaces, it is necessary to develop a novel strategy to combine nature-inspired nanoscale geometries, mechanical micro-armors, and strength-ductility balanced subsurface internal nanostructures.

In this study, we demonstrated a straightforward strategy for fabricating self-armored multi-scale hydrophobic surfaces in a flexible and large-scale fashion. The application scope of the laser shockwave was expanded, and a new technology for 3D gradient laser shock peening without coating fabrication of high-reliability hydrophobic surface structures was proposed. The hydrophobic and mechanical properties of copper were studied using the 3LSPwoC. The numerical simulation results of the finite element and molecular dynamics simulations provide theoretical support for the experimental data. The application of this technology can achieve both excellent hydrophobic and mechanical properties of metallic components, which opens avenues for high-performance and durable engineering applications.

2. Materials and methods

2.1. Urgent need of self-armored hydrophobic surfaces

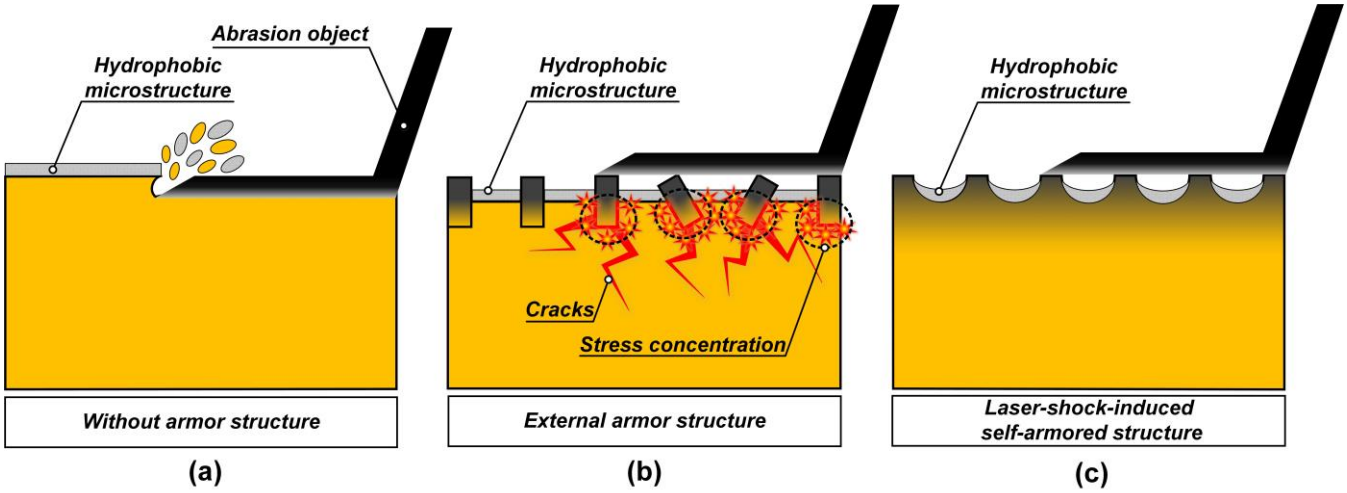

Fig. 1. Different hydrophobic surface structures. (a) hydrophobic surface without armor. (b) external armor hydrophobic surface. (c) laser-shock-induced self-armored hydrophobic surface.

In addition, the hydrophobic structure made on the power surface can reduce the drag and effectively improve the driving speed of the power. Hydrophobic metal surfaces can be fabricated by forming microstructures on metal surfaces and reducing the surface energy of the microstructure, which is a widely recognized method. Currently, the main technical bottleneck is the improvement in the mechanical strength of the hydrophobic metal structure. Under the action of high-frequency periodic external mechanical loads (such as deicing and defrosting operations and sea water scouring of ships), the hydrophobic surface structure without armor can easily fail (**Fig. 1**a). The service reliability of the hydrophobic surface of the external armor was also affected. The external armor constituted other hard materials and was embedded on the surface of the target to achieve protection. Because there were two types of materials on the target surface, stress concentrated easily at the interface of the materials, generating microcracks, which affected the service reliability of the structure (**Fig. 1**b). Therefore, the manufacture of a metal hydrophobic surface with excellent mechanical properties is an urgent problem that needs to be solved in the engineering field. Accordingly, we introduced the concept of self-armored hydrophobic surfaces (**Fig. 1**c). This metal surface is a strengthened multistage heterogeneous gradient armor structure (detailed in section 3.3 Mechanical properties), that can effectively resist the impact of external mechanical loads, protect the internal hydrophobic nanostructures, and improve the service life of the hydrophobic structure. Self-armored hydrophobic surfaces can easily be extended to different kinds of metal surfaces (detailed in section 3.4 Application to other metals), and are of high engineering value.

2.2. Materials

A copper plate with the purity of 99.99% was selected for 3LSPwoC. The thickness of the pure copper plate was 200 μm. The main elemental composition of the copper plate is listed in **Table. 1** Pre-annealing was carried out in a vacuum tube furnace at 600 ℃ for 1 h, and the heating rate of the tube furnace was 5 ℃/min. As shown in **Fig. S1**a-c, 316 stainless steel woven grids of three different sizes were used as auxiliary parts for 3LSPwoC, acting as optical masks and momentum transmission layers. The size (a*b) and thickness (d) of the thin metallic grids are shown in **Table. 2**.

Table. 1 Main element composition of copper plate

Element	Bi	As	Sb	Fe	Pb	S	Cu
Content(*wt*%)	0.0008	0.0013	0.0015	0.0036	0.0038	0.0044	Bal

Table. 2 Geometry of the thin metallic grids

Group number	a×b (μm^2)	d (μm)
Case 1	100×100	50
Case 2	150×225	70
Case 3	250×425	80

2.3. Processing setup

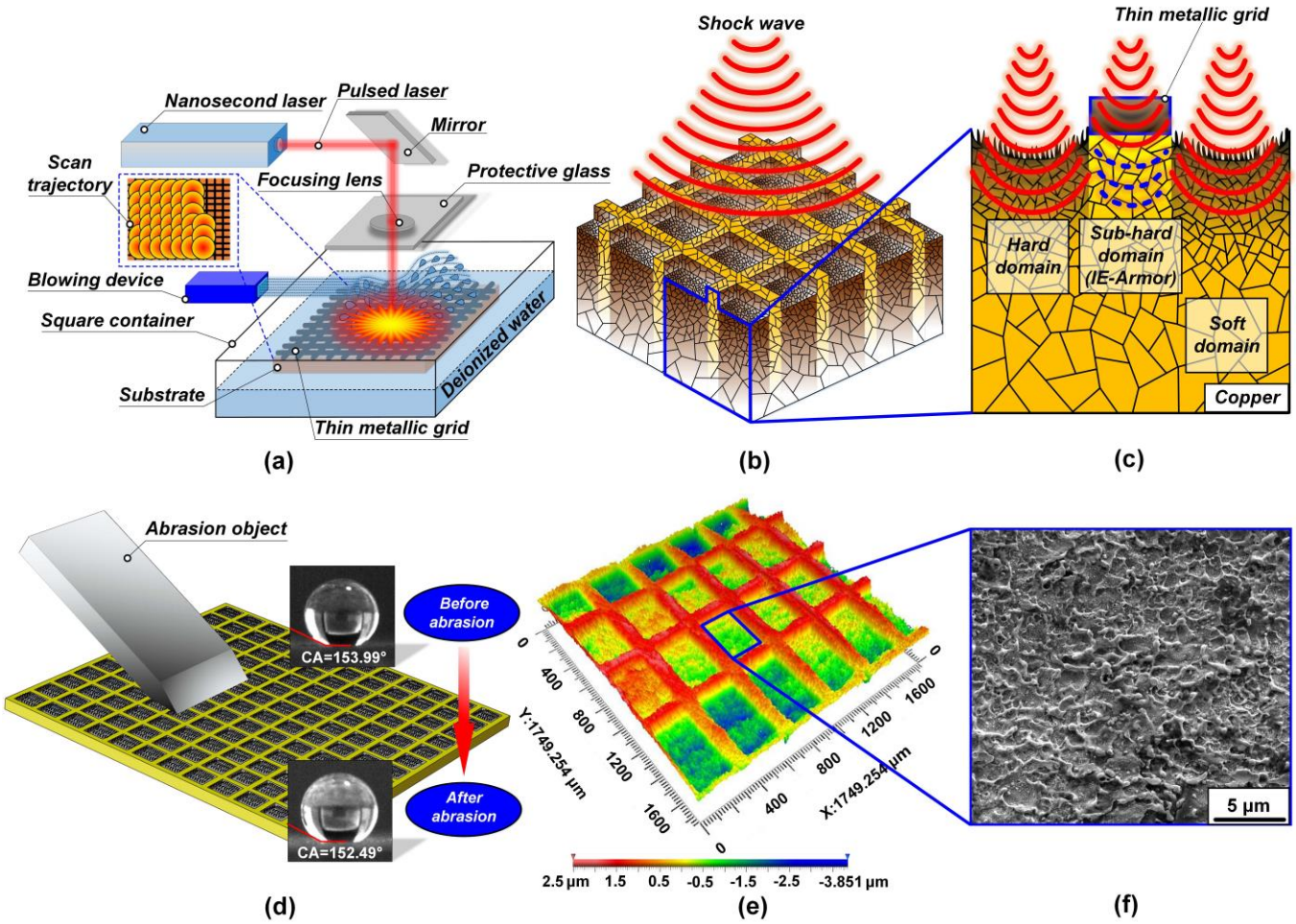

Fig. 2. Process-mechanism-application of 3LSPwoC. (a) schematic of the 3LSPwoC process. (b) 3D gradient structures fabricated by 3LSPwoC. (c) cross-sectional view of a 3D gradient structure. (d) robust hydrophobic properties of 3LSPwoC samples. (e) 3D profile topography of the 3LSPwoC sample. (f) micro-nano morphologies of 3LSPwoC samples.

Fig. 2a displays a schematic of the 3LSPwoC process. A Q-switched nanosecond Nd:YAG laser was used for laser shock experiments. A laser shock path was built in front of the laser using an optical platform. The entire optical path ensured that the nanosecond laser could be vertically irradiated on the sample surface after passing through the mirror, focusing lens, and protective glass, successively. An air blast device was placed beside the square container. The airflow generated by the blowing device was used to change the movement path of the splashing droplets under impact to prevent pollution of the mirror group and affect the beam quality. The square container was placed on a three-coordinate moving platform, which was

used to realize the spot lap of the pulse laser. The cleaned annealed copper substrate was placed in a square container, and a thin metallic grid was placed over the copper surface. The edge position of the thin metallic grid was fixed using a metal clamp, ensuring the thin metallic grid and copper are as close as possible. Deionized water was poured along the walls of the square container. The thin metallic grid was pressed slightly using a scale to squeeze out any remaining air bubbles at the bottom of the grid. The blowing device, laser, and mobile platform were then switched on successively to develop the laser shock experiment (Supplementary Video 1).

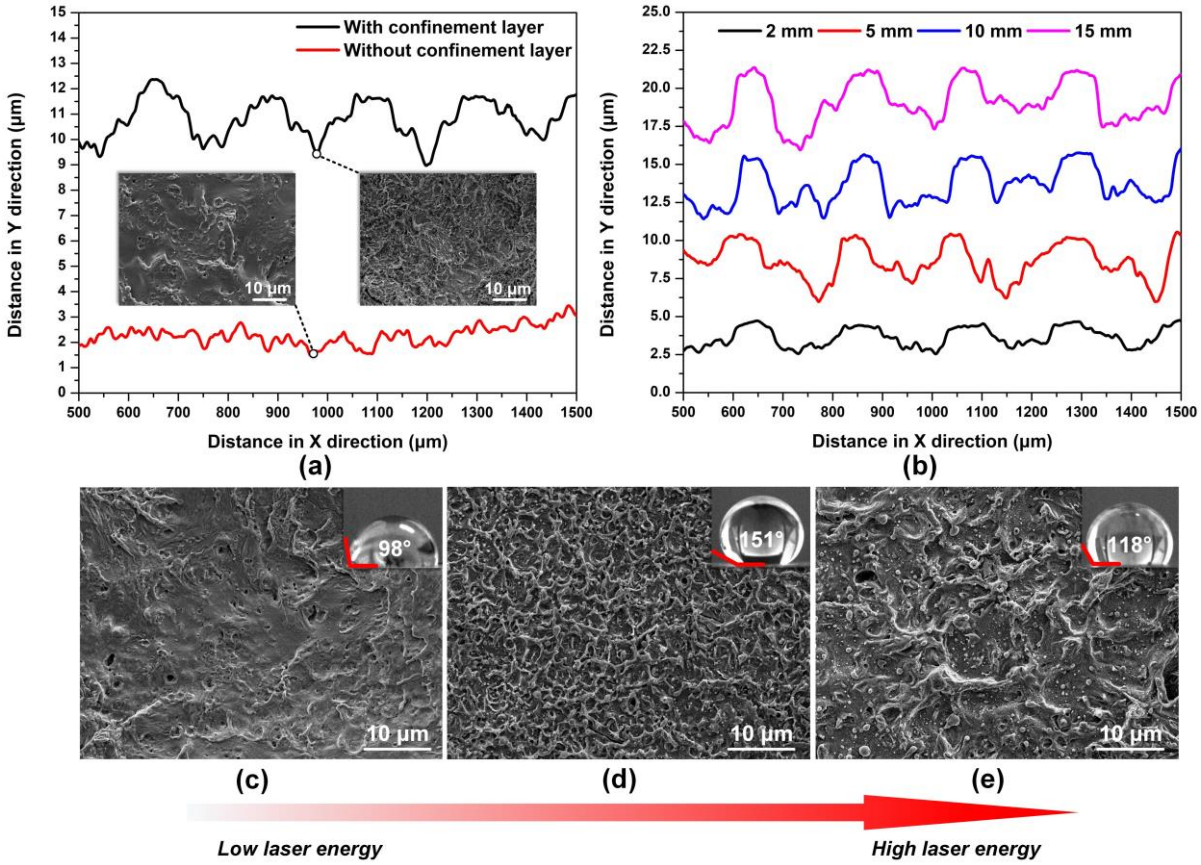

Fig. 3. Optimization of process parameters. (a) 2D profile morphology and SEM morphology of the functional structure of the sample with or without the confinement layer. (b) 2D profile of the sample surface under different thickness of confinement layer. (c) 1.2 GW·cm^{-2}. (d) 8.1 GW·cm^{-2}. (e) 16.2 GW·cm^{-2}.

The process parameters are closely related to the morphology and properties of the samples. For example, it is well known that the pulse width of a laser is related to the heat input [33,34]. To highlight the force effect of the pulse laser and improve the mechanical properties of the materials, a smaller pulse width was selected in this study. Laser scanning speed, pulse laser frequency and spot size are the three parameters that affect the spot overlap rate. By coordinating the above three parameters, the overlap rate of laser spot was finally achieved as 50%. In the early stage, we focused on the analysis of the effect of the presence or absence of the confinement layer, the thickness of the confinement layer, and the pulse laser energy on the production of samples. The shockwave induced by the pulse laser was transmitted in the thickness direction of the target under the constraint of the confinement layer. Compared with the samples without the confinement layer, the samples with the confinement layer exhibited more obvious surface fluctuations and more abundant micro-nano structures (**Fig. 3**a). The thickness of the confinement layer constrained the plasma escape, therefore, the thickness of the confinement layer affected the shock pressure. When the thickness of the constraint layer was increased from 2 mm to 10 mm, the deformation of the sample increased gradually. However, when the thickness of the confinement layer continued to increase to 15 mm, the shape variable of the sample did not significantly increase (**Fig. 3**b). Compared with the samples at low laser energy, with an increase in laser energy, the number of micro-nano structures on the material surface increased under the action of heat, force, and other comprehensive factors. However, when the laser energy was too large, the degree of disturbance of the sample surface increased owing to the obvious force effect, and the size of the micro-nano structure of the material surface increased, which impacted on the hydrophobicity of the material (**Fig. 3**c-e). Based on above experimental studies, **Table. 3** details the process parameters of the 3LSPwoC used in this study.

Table. 3 3LSPwoC process parameters

Process parameters	value
Laser wavelength (nm)	1064
Laser pulse width (ns)	7
Laser pulse frequency (Hz)	10
Single pulse energy (J)	1
Spot diameter (mm)	1.5
Scanning speed (mm·s^{-1})	20
Overlap rate of the laser spot	50%
Confinement layer material	Deionized water
Confinement layer thickness (mm)	10

2.4. Characterization methods

(1) Morphology characterization

An optical microscope (BX53M, Olympus Inc., Japan) was used to observe the macroscopic appearance of the samples. A white light interferometric 3D profiler (NewViewTM 9000, ZYGO Inc., U.S.A.) was used to observe the 3D morphology and roughness of the samples. A field emission scanning electron microscope (SEM) (MIRA 3, TESCAN Brno,s.r.o. Inc., Czech Republic) with an energy dispersive spectrometer (Aztec Energy, Oxford Instruments Nanoanalysis Inc., U.K.) was used to observe the microscopic morphologies of the samples. Transmission electron microscopy (TEM) (JEM-2100F, JEOL Inc., Japan) at the accelerating voltage of 200 kV was used to characterize the microstructure.

(2) Wettability characterization

A goniometry instrument (JCY-4, Fangrui Inc., China) was used to measure the contact angle of the sample at room temperature (25± 2 ℃) with a 4-μL distilled water droplet. For the experiment on the hydrophobicity of the material surface after dry friction, the 240-mesh sandpaper was placed on the surface of the samples and the samples were subjected to mechanical friction treatment with the weight of 100 g. Utilizing the goniometry instrument, the hydrophobic angle of the surface of the sample after the friction treatment was tested. Dry sliding friction experiments were conducted at room temperature using a friction and wear testing machine (M-2000, Henxu Inc., China) as well as 316 L stainless steel dual balls with the diameter of 6 mm.

(3) Characterization of mechanical properties

A nanoindenter (TI 950 TriboIndenter^{TM}, Bruker Inc., U.S.A.) was used to measure the hardness of the samples. The pressure load was 3000 μN, and the loading method was 5 s loading, 2 s holding the load, and 5 s unloading. The X-ray diffractometry (XRD) (X' Pert PRO, Almelo, Netherlands) was employed to analyze the phase composition and residual stress distribution trend of the samples. The XRD scan was performed using Cu Kα1 radiation (λ=0.1541 nm) in the 2θ range of 20°to 80°at the rate of 4 °/min and counting time of 1 s per step. A universal testing machine (5956, Instron Inc., U.S.A.) determine used to test the tensile properties of the samples.

2.5. Simulation methods

The mechanism of plastic deformation of annealed copper induced by laser shock was verified via molecular dynamics (MD) simulation method using a large-scale atomic/molecular massively parallel simulator (LAMMPS) [35]. A Cu model with a dimension of 40.2 nm×20.1 nm×10.1 nm was established. A periodic boundary was used in the *x*, *y*, and *z* directions. The embedded-atom method (EAM) potential was selected to describe the interaction between the Cu atoms [36]. Structural optimization was performed using a conjugate gradient algorithm. Subsequently, the model was relaxed for 50 ps in an isothermal-isobaric ensemble to obtain an equilibrium model. The strain rate for the uniaxial compression was set to 10E9 s^{-1}. Visualization of atoms and analysis of dislocations were achieved using OVITO [37]. Finite element simulation was performed to calculate the residual stress distribution and value of the 3LSPwoC samples and the tensile properties of the samples manufactured by different processes. Details of the finite element simulation can be found in sections 5-6 of the Supplementary Material.

3. Results and discussions

3.1. Surface topography

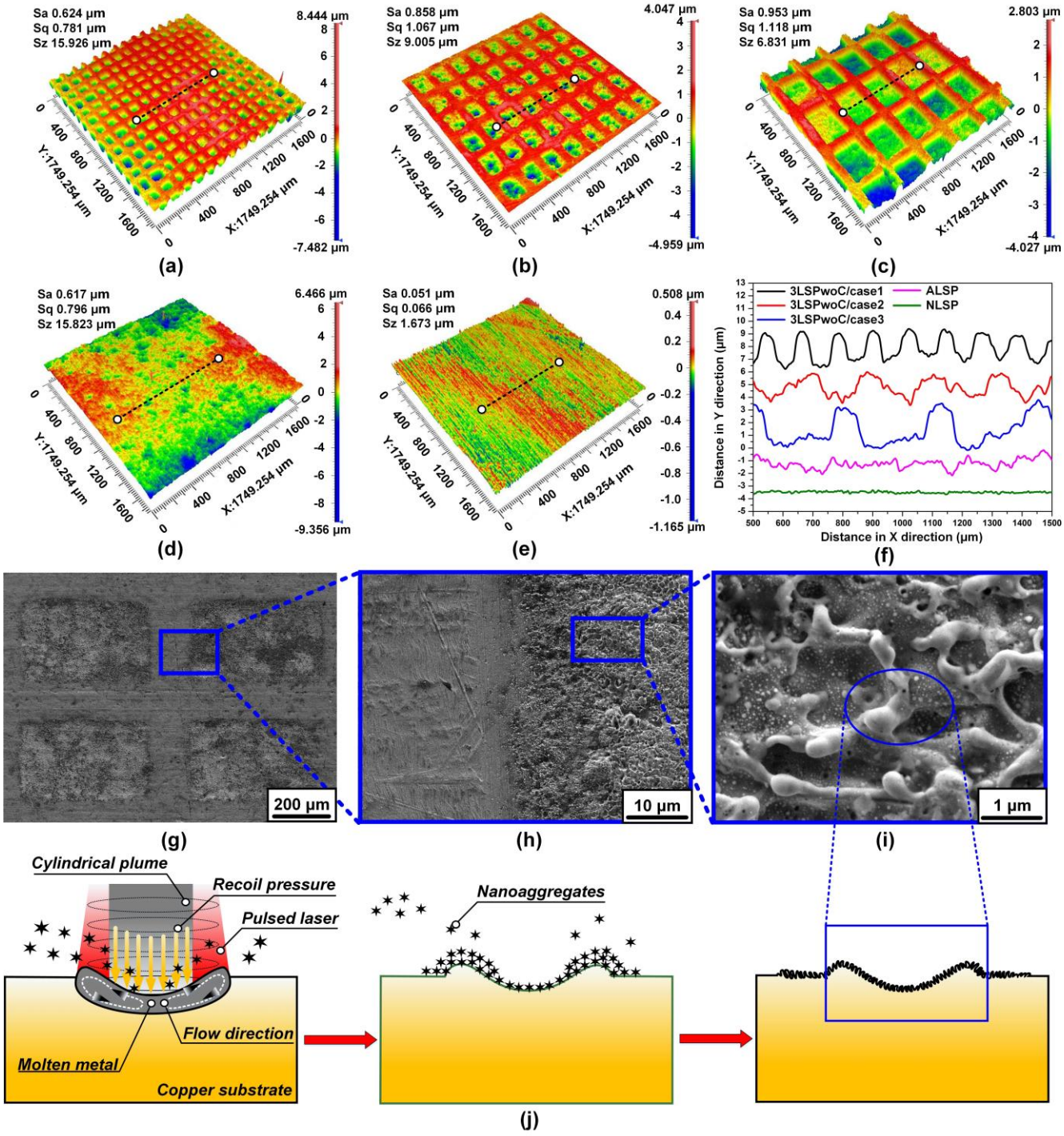

Fig. 4. Surface topographies of the samples subjected to different processes. (a) 3D profile/3LSPwoC/case1. (b) 3D profile/3LSPwoC/case 2. (c) 3D profile/3LSPwoC/case 3. (d) 3D profile/ALSP. (e) 3D profile/NLSP. (f) 2D profile of the samples under different processes corresponding to the section profile at the black dotted line in (a)-(e). (g) SEM image/3LSPwoC/case 2. (h) partially enlarged images of the blue box marked in (g). (i) partially enlarged images of the blue box marked in (h). (j) microstructure generation induced by laser shock.

The surface morphology is crucial in the fabrication of durable hydrophobic surfaces. **Fig. 4** depicts the surface topographies of the samples subjected to different processes. The surface morphologies of the 3LSPwoC samples, the samples with all-laser shock peening (ALSP), and samples without laser shock peening (NLSP) were compared. When the plasma further absorbs the laser energy and reaches the explosion threshold, it explodes and produces a shockwave on the order of GPa [38–40]. When the peak pressure of the shockwave exceeds the Hugoniot elastic limit (HEL) of the material, the surface layer of the material undergoes a plastic deformation. Under the ablation and shock of the pulse laser, part of the material on the sample surface was removed, and permanent plastic deformation occurred (**Fig. 4**a-e). The surface of the sample exhibited abundant micro- and nano-morphologies. The feasibility of plastic deformation of annealed copper and the ablation conditions are demonstrated in section 2 of the supplementary material. In contrast to the ALSP and NLSP samples, an array-like

distribution of micron-scale pits was observed on the surface of the 3LSPwoC sample, which was attributed to the interaction of the laser-induced multistage shockwave within the material. With an increase in the size of the metal grid, the ablation percentage in the unit area gradually increased. Observing **Fig. 4**f, it was found that, compared with the traditional ALSP process, 3LSPwoC could produce approximately several microns of undulations per pulse on the sample surface. The strain values of cases 1-3 in 3LSPwoC samples were ~1.19%, ~1.22% and ~1.98%, respectively. The strain value of the ALSP sample was ~0.78%. Combined with the 3D and 2D profiles, the volumes of the 3LSPwoC samples under different conditions were estimated. As the size of the metal grid increased, the volume of the micro-pits increased from 2×10^4 μm^3 in case 1 to 3×10^5 μm^3 in case 3. The microscopic morphologies of different regions of the 3LSPwoC samples varied. As shown in **Fig. 4**g-i, the pits directly interacting with the laser had abundant corrugated micro- and nano-morphologies, including nanospheres, nanoholes, and nanogrooves. As shown in **Fig. 2**j, the rapid evaporation of the surface materials and phase explosion led to the formation of a laser-induced plume. The atmospheric environment limited the free expansion of the laser-induced cylindrical plume, which led to intensified collisions between the products induced by the pulse laser and surrounding matter. Vigorous collisions between the species further led to the aggregation and oxidation of these laser-ablated species and the formation of complex nanoaggregates. These nanoaggregates reacted with the surface molten layer and were eventually redeposited back to the substrate surface, forming a complex microstructure. Compared with traditional ALSP and NLSP samples, 3LSPwoC could induce more apparent surface fluctuations, and obtain arrayed pits with rich micro-nano structures.

3.2. Surface wettability

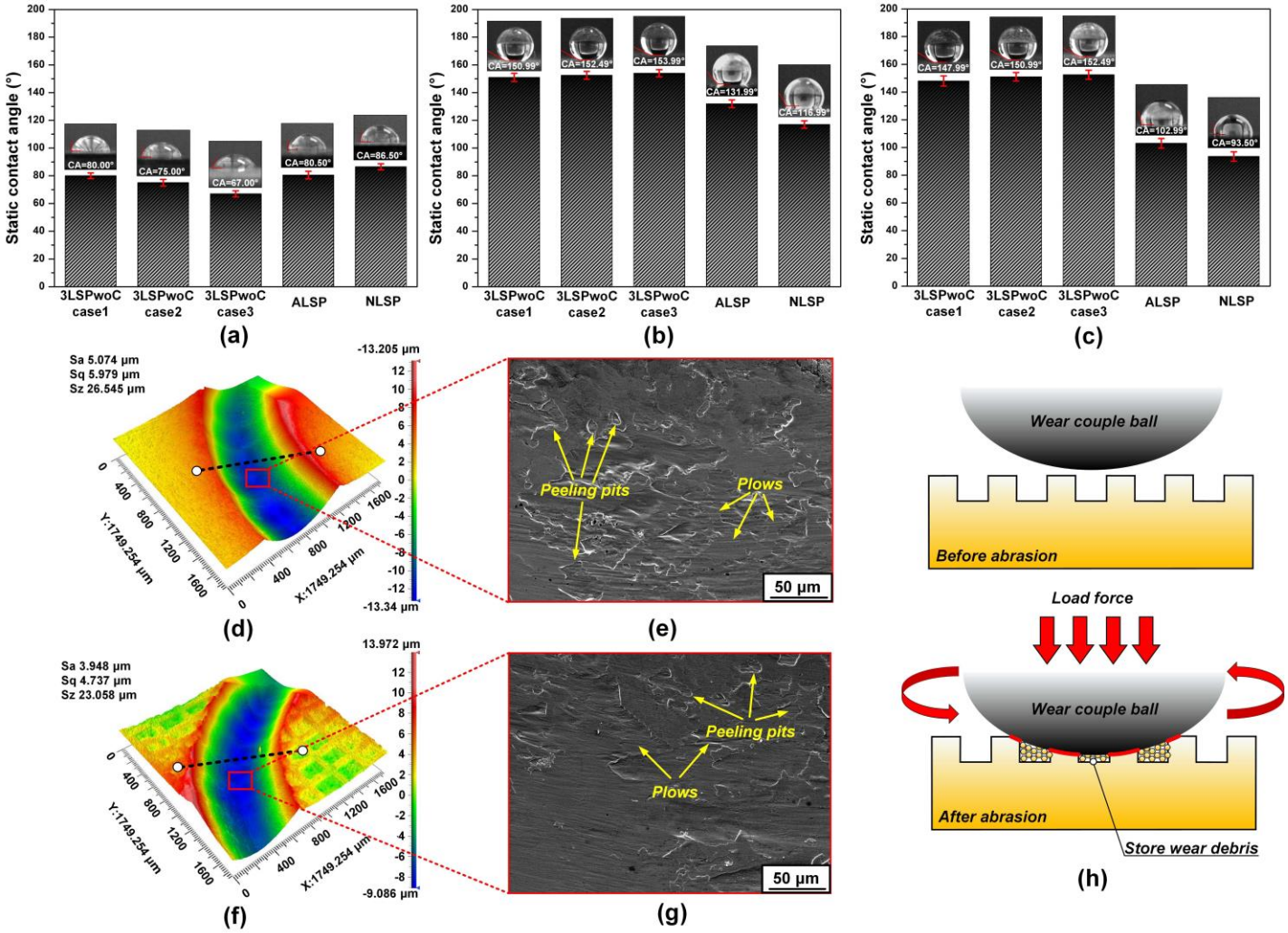

Fig. 5. Contact angles of the samples fabricated using different processes. (a) static contact angle of the original samples. (b) static contact angle of the sample after coating chemical reagents. (c) static contact angle of the sample after abrasion. (d) 3D contours of the wear marks of the NLSP sample. (e) SEM of the abrasion marks of the NLSP sample. (f) 3D contours of the wear marks of the 3LSPwoC sample. (g) SEM of the abrasion marks of the 3LSPwoC sample. (h) wear resistance mechanism of 3LSPwoC sample.

The samples manufactured using the 3LSPwoC process were tested for durable hydrophobicity. **Fig. 5** presents the contact angles of the samples fabricated using different processes. As shown in **Fig. 5a,** the surfaces of the samples fabricated

by the different processes were hydrophilic before coating with low-surface-energy reagents. The static contact angles of the samples were NLSP, ALSP, and 3LSPwoC, in descending order. As the size of the metal grid increased, the contact angle of the sample gradually increased. As shown in **Fig. 5**b, the surfaces of the samples became hydrophobic after coating with the low-surface-energy reagents. It was worth noting that the samples fabricated via the 3LSPwoC process were in a superhydrophobic state. The static contact angles of the samples are in descending order for 3LSPwoC, ALSP, and NLSP. As the size of the metal grid increased, the contact angle of the sample gradually increased. The wettability of the samples manufactured using different processes after abrasion was tested by designing abrasion experiments. As shown in **Fig. 5**c**,** after abrasion, the static contact angles of the ALSP and NLSP samples decreased sharply by approximately 20-30°, whereas the 3LSPwoC samples maintained excellent hydrophobic stability with a decrease of approximately 1-3°, and 3LSPwoC/case2 and 3LSPwoC/case3 still maintained a superhydrophobic state. The microstructure and chemical composition of the material surface are the main factors that affect the wettability of the solid surface. Currently, the Wenzel and Cassie models are two common theoretical models used to describe the roughness of a material surface [41,42]. When the surface of the material was not wetted, the liquid was in contact with every part of the rough surface in the Wenzel state. In the Cassie state, the liquid was suspended on the grooves of the rough surface but could not fill the grooves of the rough surface, and only came into contact with the convex surface of the rough surface. Nanosecond pulsed laser textured material surfaces would produce abundant micro- and nano-structures. The microstructure spontaneously forms hydrophilic chemical groups. After the sample was soaked in a chemical reagent with low surface energy, the fluorinated groups with low binding energy were adsorbed on the surface of the microstructure, and chemical reactions occurred, thus changing the wettability of the material surface and making the surface of the material appear hydrophobic. The ALSP sample is in a typical Wenzel hydrophobic state. Meanwhile, the 3LSPwoC sample was typical of the Cassie hydrophobic state, which was attributed to an array of pits on the surface of the 3LSPwoC sample. These pits become stable gas storage sites. In the Cassie state, the apparent contact angle increases significantly, making it easier to achieve a superhydrophobic state. The wear of the NLSP and 3LSPwoC samples under mechanical loading is depicted in **Fig. 5**d-g. The wear morphology of the NLSP samples was accompanied by deep plows and numerous peeling pits. However, the depth of the plows and the number of peeling pits in the 3LSPwoC samples were significantly reduced. The friction coefficient of the 3LSPwoC sample is lower than that of the NLSP sample (**Fig. S4**a), and the wear amount and abrasion depth were further reduced (**Fig. S4**b-c). The reinforced surface of the 3LSPwoC samples improved the resistance to external mechanical loads, and the arrayed pits became the storage place of wear debris **Fig. 5**h, which reduced the damage caused by wear debris to the surface morphology. The 3LSPwoC process could obtain metal surfaces with stable and durable hydrophobic properties under the influence of abrasion owing to the multi-scale surface structuring effect (Supplementary Video 2).

3.3. Mechanical properties

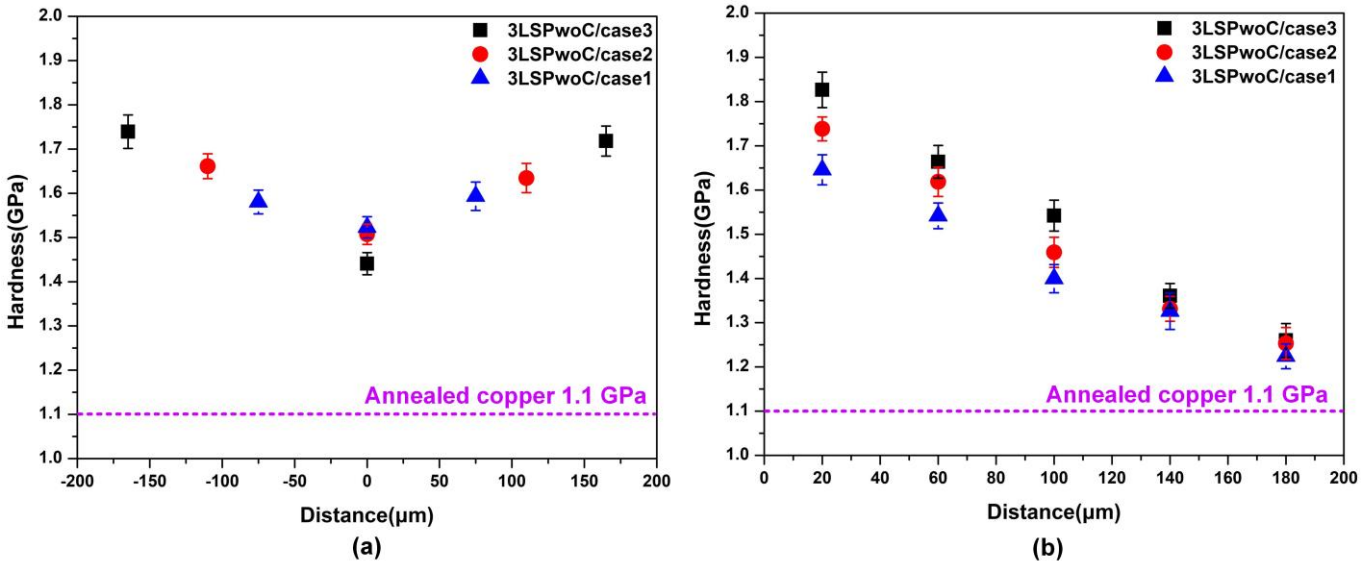

Fig. 6. Nanoindentation test results of 3LSPwoC samples. (a) horizontal direction. (b) vertical direction.

The mechanical properties of materials manufactured by different processes were explored further through indentation tests, uniaxial tension, and other characterizations and relevant simulations. The 3D gradient distribution of the mechanical properties is shown from in the nanohardness tests in of **Fig. 6**. Detailed indentation position, loading, and unloading curves

are provided in **Fig. S5**. As shown in **Fig. 6**a, the hardness of the material under the metal grid (distance of 0 μm) was smaller than that directly acted upon by the laser, which was attributed to the reduction in the peak energy of the shockwave. The hardness in the horizontal direction of the sample exhibited clear gradient changes. With an increase in the size of the metal grid, the hardness of the area directly affected by the laser increased gradually. As shown in **Fig. 6**b, the hardness of the sample gradually decreased with increasing of depth. However, at the same depth, the hardness gradually increased with an increase in the size of the metal grid, which was attributed to an increase in the plastic deformation of the sample. When the distance was 180 μm, the hardness of the sample was close to that of annealed copper (**Fig. S5**g). Comparing **Fig. 6**a-b, it was found that the 3LSPwoC process could produce a structure with an alternating hardness distribution on the surface of the sample. Compared with the hardness of the original annealed copper, the material under the metal grid was also strengthened, and the hardness was increased by 25%. On the one hand, 3LSPwoC fabricated an IE-armor structure, and on the other hand, 3LSPwoC fabricated a 3D structure with a gradient of mechanical properties along the horizontal and vertical directions.

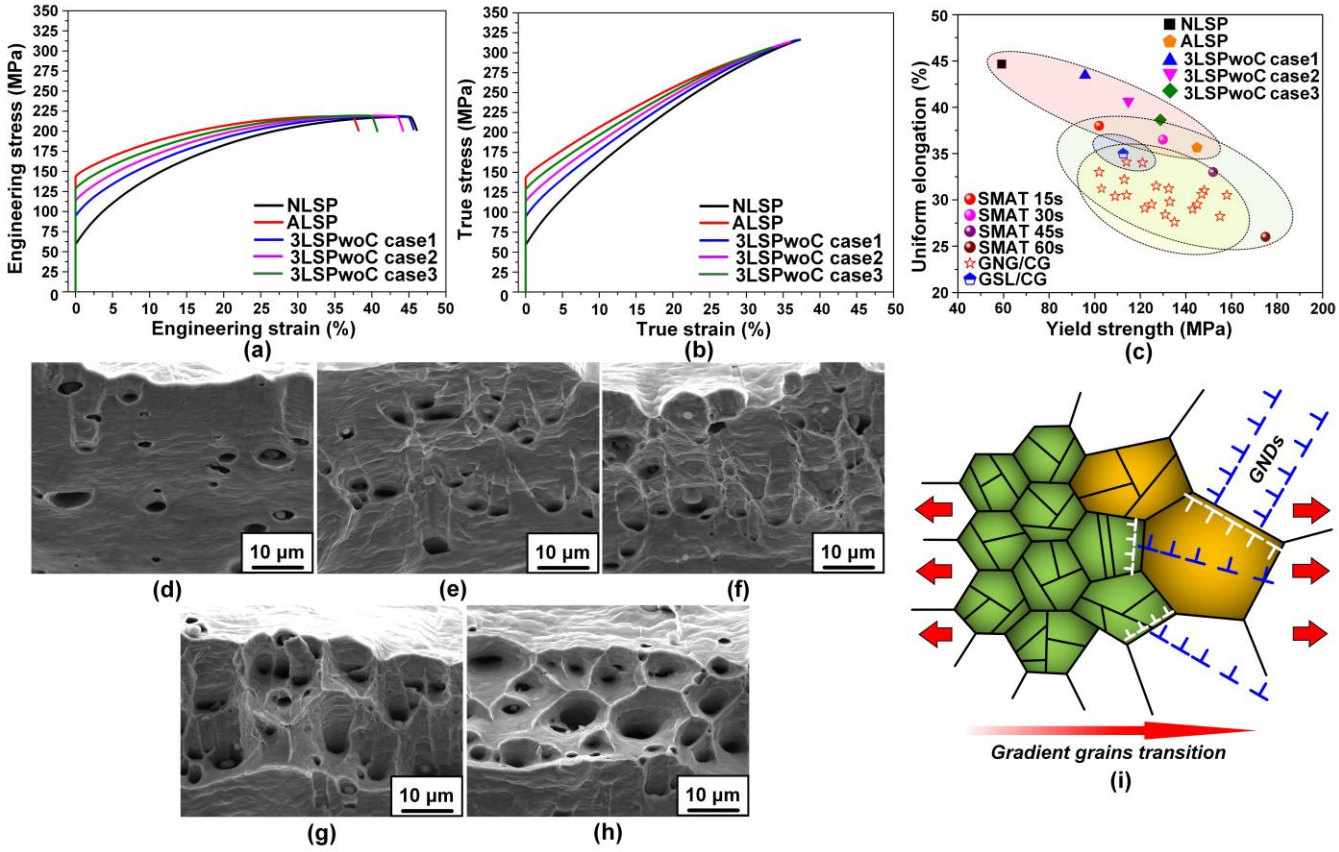

Fig. 7. Tensile properties of samples fabricated using different processes. (a) engineering stress-engineering strain curves. (b) true stress-true strain curves. (c) yield strength and uniform elongation of tensile samples under different processes. (d) ALSP sample. (e) 3LSPwoC sample/case3. (f) 3LSPwoC sample/case2. (g) 3LSPwoC sample/case1. (h) NLSP sample. (i) synergistic mechanism of strength and ductility.

The tensile properties of the 3D gradient structures fabricated using the 3LSPwoC process are shown in **Fig. 7**. NLSP samples exhibited high ductility (~44%) and low strength (~60 MPa), while ALSP samples exhibited low ductility (~36%), high strength (~145 MPa). In contrast, the 3LSPwoC samples exhibited a better coordination of strength and ductility. The 3LSPwoC/case1 sample exhibited a significant increase in yield strength (~96 MPa) with little sacrifice in ductility (~43%). Compared with the NLSP sample, the strength of the 3LSPwoC sample was improved, and compared with the ALSP sample, the ductility of the 3LSPwoC sample was improved. Further, regarding the 3LSPwoC sample, the yield strength of the material gradually increased, and the ductility decreased gradually with an increase in of the size of the metal grid, which was attributed to the increase in plastic deformation caused by the enlargement of the laser direct impact area. Compared with the SMAT [32], GNG/CG [43], and GSL/CG [44] processes, the 3LSPwoC process shows good balanced tensile properties owing to its ultrahigh strain rate effect. The fracture morphology of the tensile samples could indirectly reflected the strength and ductility of the material. Observing **Fig. 7**d-h, it was found that the fracture morphologies of the different samples comprised faults and dimples. The areas occupied by the discontinuities and dimples varied among the samples. The ALSP samples exhibited more fault morphologies and fewer dimples morphologies. Meanwhile, the NLSP samples had fewer fault and more

dimple morphologies. For the 3LSPwoC sample, with an increase in the size of the metal grid, the dimple morphology in the fracture of the sample gradually decreased, balancing the intergranular brittle and ductile fractures. The 3LSPwoC sample had a novel 3D heterogeneous gradient structure. This was mainly manifested in the gradient change in the microstructure and mechanical properties in the horizontal and vertical directions of the sample. During the tensile tests of the 3LSPwoC samples, the mechanical behavior responses of the different domains varied. Owing to the different orders of plastic deformation, there was an evident plastic strain gradient inside the material. The plastic strain gradient must be accommodated by geometrically necessary dislocations (GNDs) (**Fig. 7**i). The GNDs generated a long-range stress toward the source of the dislocation, namely the back stress, which gradually increased the strength of the soft and sub-hard domains, resulting in collaborative strengthening between the heterogeneous structures [45–47]. Therefore, compared with the traditional 2D heterogeneous gradient structure, the sample manufactured using the 3LSPwoC process had a larger strain gradient. The increase in back stress would more effectively prevent premature necking of the material in the tensile process, and realize a synergistic response of strength and ductility.

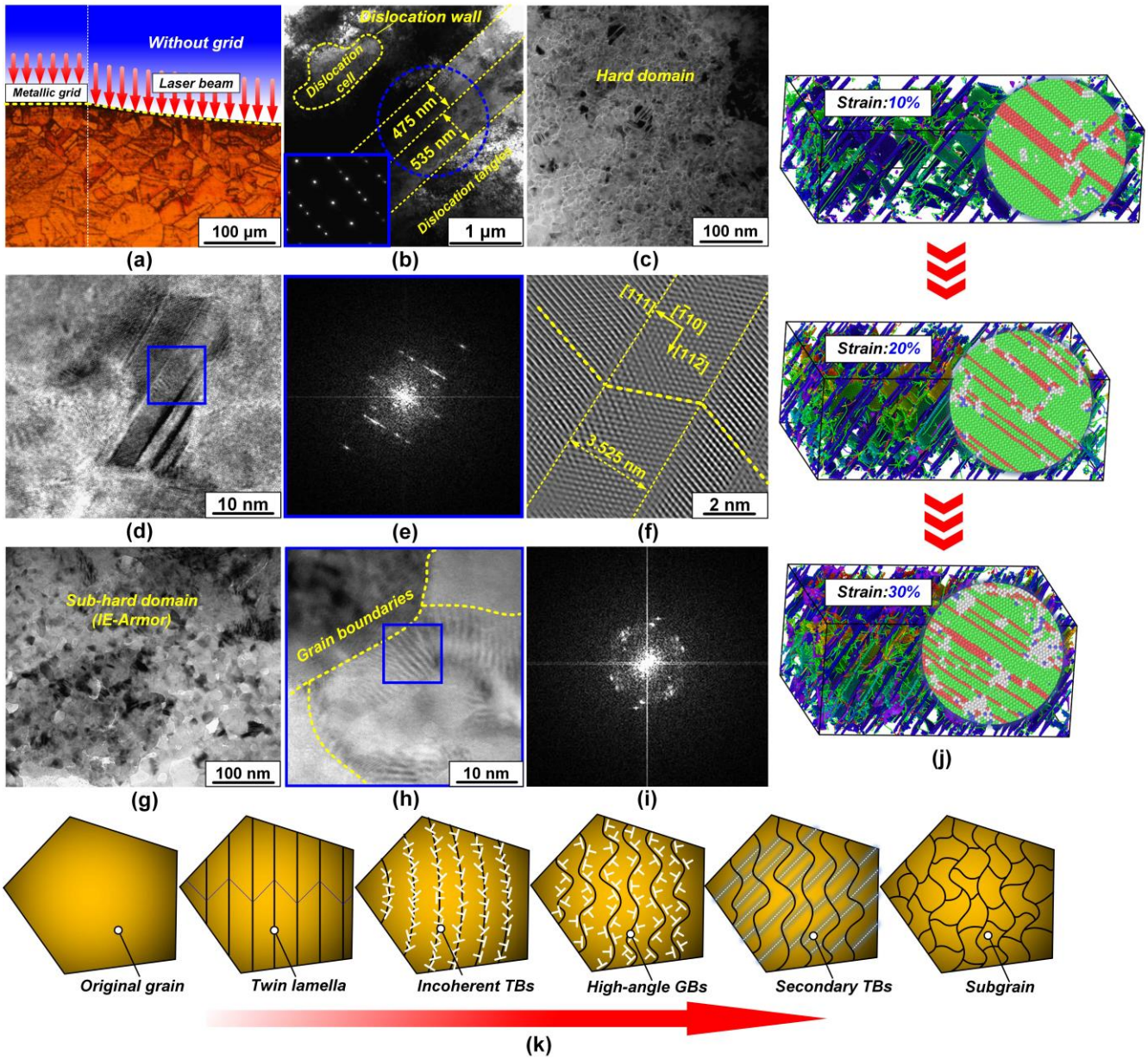

Fig. 8. Strengthening mechanism of 3LSPwoC process. (a) OM image of the cross-section of the 3LSPwoC sample. (b) TEM morphology of soft domain. (c) TEM morphology of hard domain. (d) HRTEM morphology of (c). (e) selected area electron diffraction pattern of blue box region in (d). (f) inverse Fourier transform (IFFT) image of (e). (g) TEM morphology of sub-hard domain (IE-armor). (h) HRTEM morphology of (g). (i) selected area electron diffraction pattern of blue box region in (h). (j) variation process of twin spacing in materials during laser shock. (k) grain refinement mechanism based on TBS and stacking faults.

The size of the grains is related to the hardness of a material within a certain range according to the Hall-Petch theory

[48]; that is, the hardness of the material increased gradually as the grain size decreased. **Fig. 8** shows the microstructural changes after the 3LSPwoC process. **Fig. 8**a presents an OM image of the cross-section of the 3LSPwoC sample. Under the interaction between the laser-induced shockwave and material, grain refinement occurred at the subsurface of the material. **Fig. 8**b–i show the plastic deformation mechanisms of the 3LSPwoC samples. A large number of obvious nanograins were observed in the sub-hard domain (IE-armor) and hard domain. It was worth noting that the nanograins of the hard domain were smaller than those of the sub-hard domain. Compared with the twin spacing in the soft domain (~500 nm), the twin spacing in the hard domain was further reduced to approximately 3 nm, which was attributed to the strain gradient in the thickness direction of the sample. The calculated results of MD (**Fig. 8**j) were consistent with the TEM data, which was mainly reflected in the variation trend of twin spacing; that is, with the decrease in shock pressure in the direction of material thickness, the strain decreased and the twin spacing increased. **Fig. 8**k depicts the grain refinement mechanism based on the TBS and stacking faults. The original grain was split into twin lamellae by a partial dislocations emitted from grain boundaries (GBs). Dislocations piled up at the twin boundaries (TBs) convert coherent TBs to incoherent TBs. As the strain increases, the incoherent TBs switch to large-angle GBs and generated a new dislocation source at the GBs. With further deformation, partial dislocations are emitted from the new GBs, forming secondary deformation twins. The secondary TBs and newly generated GBs form a cross-distributed rhombic lattice region [49]. Subsequently, the secondary TBs transformed into the incoherent GBs with high angles, and refined sub-grains were formed.

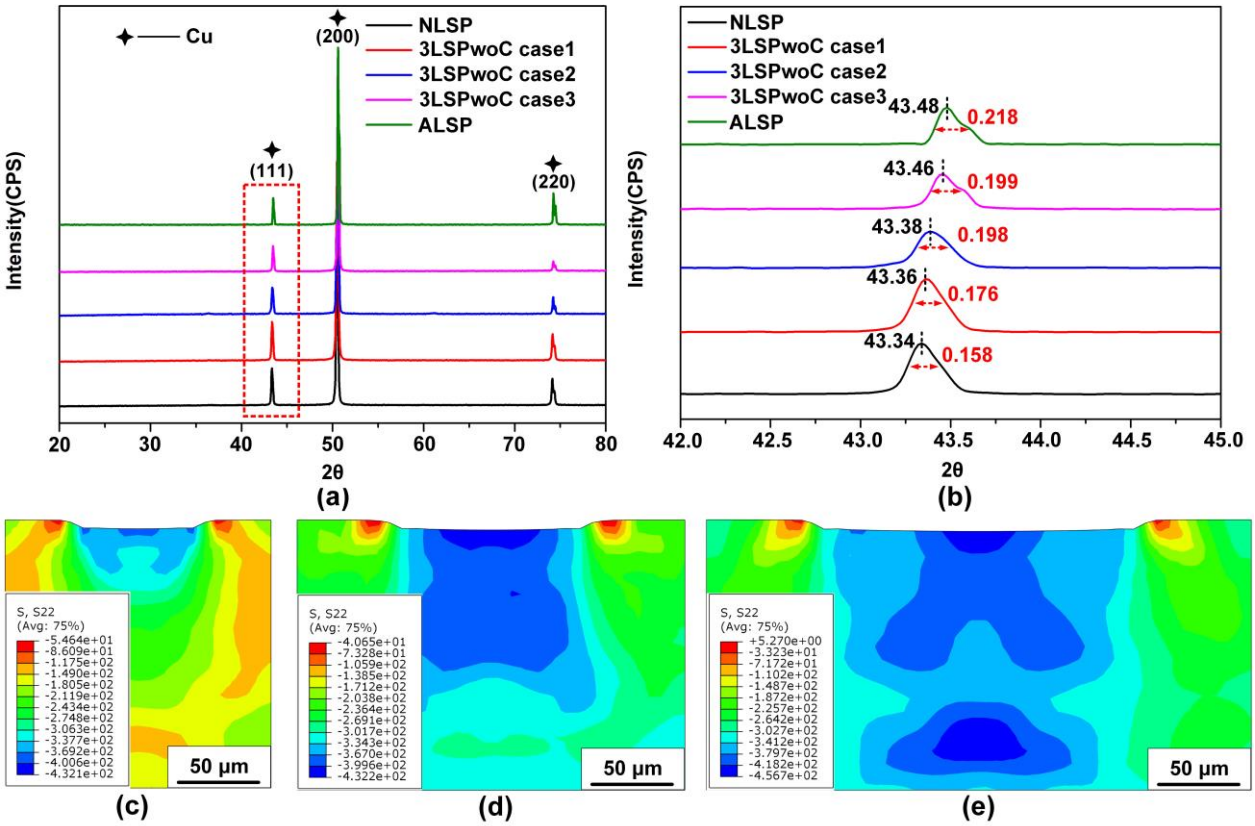

Fig. 9. XRD patterns and residual stress calculation results. (a) overall XRD image. (b) partial enlarged image in red dotted box of (a). (c) 3LSPwoC sample/case1. (d) 3LSPwoC sample/case2. (e) 3LSPwoC sample/case3.

The XRD test results provided evidence of the phase composition and stress distribution state of the samples under different processes. **Fig. 9**a presents the XRD patterns of samples under different processes. Only a single Cu component was detected in the 3LSPwoC and ALSP samples, and no obvious oxidation phenomenon was observed, indicating that the laser shock did not change the composition of the material. The full width at half maximum (FWHM) and the offset of the diffraction peaks were used to evaluate the stress state of the material [50]. The spacing of the crystal planes varied with the residual stress. **Fig. 9**b partially magnifies the diffraction peak of the (111) crystal plane. The FWHM and offset of the diffraction peaks were ALSP, 3LSPwoC, and NLSP, respectively, in descending order. For the 3LSPwoC sample, with an increase in the size of the metal grid, the FWHM and shift of the diffraction peak gradually increased. After the laser shock, the (111) crystal plane of the samples shifted to higher angles, which is attributed to the reduction in the interplanar spacing by residual compressive stress. The XRD test results are similar to the simulation results, verifying the validity of the model. Residual stress also affected the hardness of the material [51], and the finite element calculation results verified the

distribution area and magnitude of residual stress in the 3LSPwoC sample under different conditions (**Fig. 9**c-e). With the increase in the size of the metal grid, the distribution area and value of the residual compressive stress increased, which was attributed to the increase of the energy after the multiple reflection of the shockwave with the increase in the size of the metal grid. The distribution and value of the residual stress were consistent with the hardness of the sample.

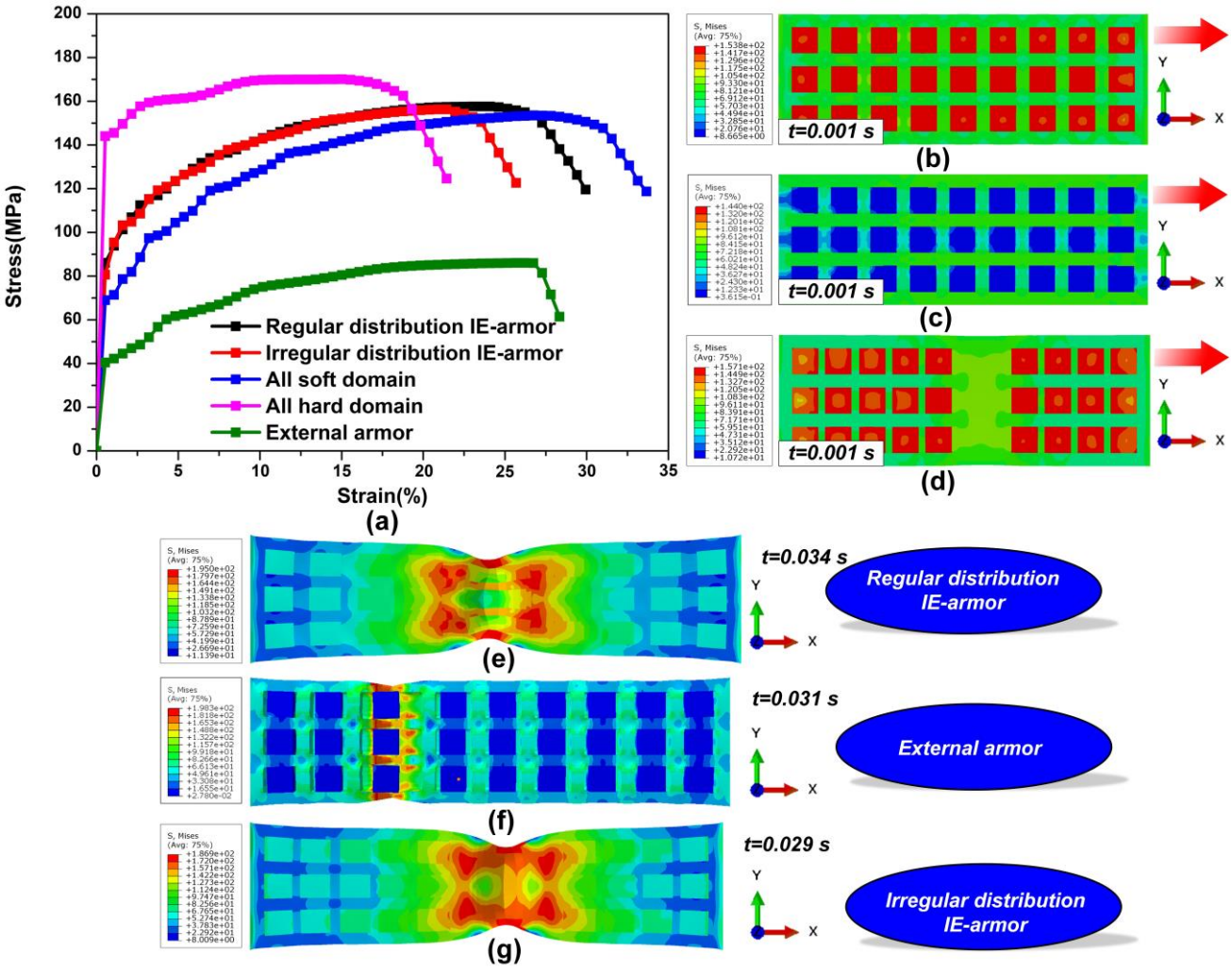

Fig. 10. Mechanisms of gain in tensile properties of 3LSPwoC samples. (a) stress-strain curve obtained by numerical simulation without consideration of twining. (b) initial tensile state of the regular distribution IE-armor. (c) initial tensile state of the external armor. (d) initial tensile state of irregular distribution IE-armor. (e) initial necked state of the regular distribution IE-armor. (f) initial necked state of the external armor. (g) initial necked state of irregular distribution IE-armor.

Numerical simulations were used to illustrate the property enhancement mechanisms of the tensile properties (**Fig. 10**) of the 3LSPwoC samples. The influence of the distribution of the 3D gradient structure on the tensile properties of the material was studied using the finite element method. The tensile tests of the material under the five conditions of all soft domains (NLSP), all hard domains (ALSP), alternating regular distribution IE-armor, irregular distribution IE-armor, and external armor were simulated. To simplify the calculation, twinning was not considered, and when establishing the alternately distributed IE-armor model, whether it was regularly or irregularly distributed, the sub-hard domain was not considered, and only the tensile properties of the structure were evaluated. It should be noted that the strength of the material was lower than that in the actual situation because of the negligible influence of the sub-hard domain and twinning. When the material was soft, it exhibited high ductility and low strength, whereas when the material was in the hard domain, it exhibited low ductility and high strength. When the surface had a distribution of hard and soft domains, the sample exhibited a balance between strength and ductility. The initial state and initial necked morphology corresponding to all hard and soft domains are shown in **Fig. S9**.

Excessive shear stress is one of the main factors affecting the tensile failure of metals. The gradient distribution of the grain size could generate macroscopic strain gradients and convert unidirectional stress into multiaxial stress to reduce strain localization. Compared with the 2D gradient structure, the 3D gradient structure exhibited better synergistic plastic deformation ability. Compared with the non-regular 3D gradient structure, the regularly distributed 3D gradient structure can

introduce additional uniform tensile stress perpendicular to the tensile direction, thereby effectively avoiding early necking and obtaining better ductility. It is worth noting that the alternately regular IE-armor structure had larger ductility than the irregularly distributed IE-armor structure. The external armor structure, owing to the weak bonding of the microstructure to the bulk material, had an earlier necking time than the alternately regularly distributed IE-armor structure, resulting in poorer tensile properties.

3.4. Application to other metals

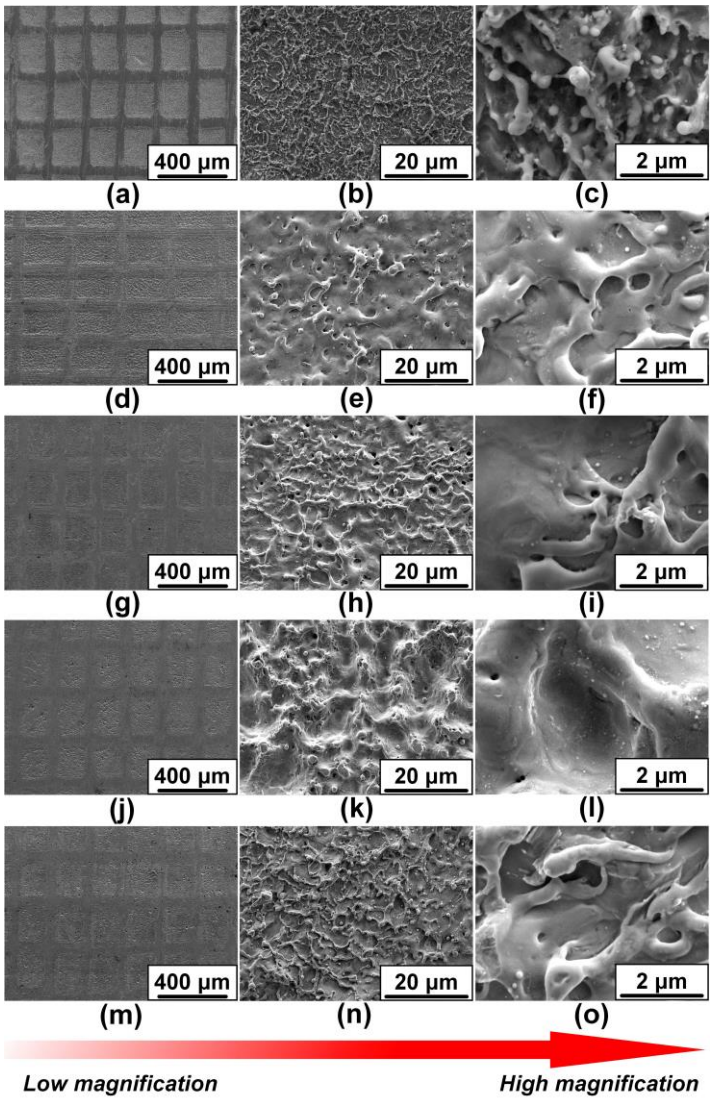

Fig. 11. 3D gradient structures fabricated on different material surfaces using 3LSPwoC process. (a)-(c) 3D gradient structure of 7075 aluminum alloy surface. (d)-(f) 3D gradient structure of Ti6Al4V titanium alloy surface. (g)-(i) 3D gradient structure of 304 stainless steel. (j)-(l) 3D gradient structure of FeCoCrNi high-entropy alloy surface. (m)-(o) 3D gradient structure of DD406 single crystal superalloy surface.

Fig. 11 displays the 3D gradient structures fabricated on the surfaces of different materials using the 3LSPwoC process. Cross-scale micro-nanocomposite structures were formed on the surfaces of different materials. The IE-armor microstructures strongly protect the nanostructures inside the arrayed micropits. The experimental data prove that the 3LSPwoC process can be applied to other metals and has excellent universality. Furthermore, we could control the roughness of the material surface and the geometric size of the gradient structure by adjusting the process parameters of 3LSPwoC (such as laser parameters or metallic grid size), and then obtain 3D gradient functional structures suitable for different service environments.

4. Conclusions

Gradient structures are considered to have excellent mechanical, physical, and chemical properties, and are widely used in aerospace, ocean engineering, locomotive manufacturing, medical treatment, transportation, energy, and other fields. In this study, we proposed a 3LSPwoC technique for manufacturing 3D gradient metal structures. An excellent application of this method is in the manufacture of self-armored hydrophobic surfaces. The microstructure, hydrophobic properties, and

mechanical properties of the 3LSPwoC, ALSP, and NLSP samples were analyzed and characterized. The application of different metals has proven the effectiveness, feasibility, and universality of the process. The main conclusions are as follows:

(1) The hydrophobic properties of the 3LSPwoC samples were better than those of the traditional ALSP samples, which was attributed to the array distribution of micropits on the surface. Nanosecond laser-induced plasma shockwaves produce micron-scale plastic deformation and micro-nanostructures. Microstructures became attachment sites for fluorinated groups with low binding energy, thus becoming potential air pockets, which reduced the liquid-solid contact area and achieved a stable Cassie state. In the friction process, the raised sub-hard domain of the 3D gradient metal structures became an integrated enhanced armor, which effectively protected the hydrophobic nanostructures inside the micropits; thus, the 3LSPwoC samples could obtain stable hydrophobic performance.

(2) The hardness of the 3D gradient metal structure varied with the gradient in the horizontal and vertical directions, indicating excellent synergistic plastic deformation ability. The yield strength of the material increased by 63%, from 59 MPa to 96 MPa, whereas the ductility decreased by only 0.4%. The 3LSPwoC sample had a multistage heterogeneous gradient structure constituting hard, sub-hard, and soft domains. In the tension process, an obvious plastic strain gradient was generated inside the heterogeneous structure, and then back stress formed, so the material produced apparent work hardening and the synergistic response of material strength and ductility was realized.

(3) The 3D gradient metal structure can be easily extended to other metallic materials that are suitable for the fabrication of mechanically robust functional surfaces with complex curved structures. Compared with the conventional laser shock peening process, 3LSPwoC is more competitive in the fabrication of high-reliability functional structures. The 3D gradient metal structure manufactured via the 3LSPwoC process is expected to play a key role in the fields of high-end CNC machine tools, aerospace, ocean engineering equipment, advanced rail transit equipment and high-performance medical instruments.

References

[1] A. Michaelides, K. Morgenstern, Ice nanoclusters at hydrophobic metal surfaces, Nat. Mater. 6 (2007) 597–601. https://doi.org/10.1038/nmat1940.

[2] Q. Gan, H. Liu, S. Zhang, F. Wang, J. Cheng, X. Wang, S. Dong, Q. Tao, Y. Chen, P. Zhu, Robust Hydrophobic Materials by Surface Modification in Transition-Metal Diborides, ACS Appl. Mater. Interfaces. 13 (2021) 58162–58169. https://doi.org/10.1021/acsami.1c17631.

[3] I. Rosenhek-Goldian, N. Kampf, J. Klein, Trapped Aqueous Films Lubricate Highly Hydrophobic Surfaces, ACS Nano. (2018). https://doi.org/10.1021/acsnano.8b04735.

[4] T. Han, Z. Ma, D. Wang, Biofouling-Inspired Growth of Superhydrophilic Coating of Polyacrylic Acid on Hydrophobic Surfaces for Excellent Anti-Fouling, ACS Macro Lett. 10 (2021) 354–358. https://doi.org/10.1021/acsmacrolett.0c00860.

[5] D. Jin, Z. Di, K. Pan, M. Xiong, F. Yang, S. Wei, Hydrophobicity of Cr3C2-NiCr coating under mechanical abrasion and thermal annealing, Appl. Surf. Sci. 574 (2022) 151600. https://doi.org/10.1016/j.apsusc.2021.151600.

[6] H. Daneshmand, A. Sazgar, M. Araghchi, Fabrication of robust and versatile superhydrophobic coating by two-step spray method: An experimental and molecular dynamics simulation study, Appl. Surf. Sci. 567 (2021) 150825. https://doi.org/10.1016/j.apsusc.2021.150825.

[7] P. Salehikahrizsangi, K. Raeissi, F. Karimzadeh, L. Calabrese, E. Proverbio, Highly hydrophobic nickel and nickel-tungsten coatings: Microstructural and surface properties, Appl. Surf. Sci. 520 (2020) 146319. https://doi.org/10.1016/j.apsusc.2020.146319.

[8] D.J. Krug, R.M. Laine, Durable and Hydrophobic Organic-Inorganic Hybrid Coatings via Fluoride Rearrangement of Phenyl T12 Silsesquioxane and Siloxanes, ACS Appl. Mater. Interfaces. 9 (2017) 8378–8383. https://doi.org/10.1021/acsami.6b16121.

[9] P. Wang, C. Li, D. Zhang, Recent advances in chemical durability and mechanical stability of superhydrophobic materials: Multi-strategy design and strengthening, J. Mater. Sci. Technol. 129 (2022) 40–69. https://doi.org/10.1016/j.jmst.2022.01.045.

[10] P. Wang, X. Yan, J. Zeng, C. Luo, C. Wang, Applied Surface Science Anti-Reflective superhydrophobic coatings with excellent durable and Self-cleaning properties for solar cells, Appl. Surf. Sci. 602 (2022) 154408. https://doi.org/10.1016/j.apsusc.2022.154408.

[11] D. Wang, Q. Sun, M.J. Hokkanen, C. Zhang, F.Y. Lin, Q. Liu, S.P. Zhu, T. Zhou, Q. Chang, B. He, Q. Zhou, L. Chen, Z. Wang, R.H.A. Ras, X. Deng, Design of robust superhydrophobic surfaces, Nature. 582 (2020) 55–59. https://doi.org/10.1038/s41586-020-2331-8.

[12] V. Vercillo, S. Tonnicchia, J.M. Romano, A. García-Girón, A.I. Aguilar-Morales, S. Alamri, S.S. Dimov, T. Kunze, A.F. Lasagni, E. Bonaccurso, Design Rules for Laser-Treated Icephobic Metallic Surfaces for Aeronautic Applications, Adv. Funct. Mater. 30 (2020). https://doi.org/10.1002/adfm.201910268.

[13] S. Mekhiel, P. Koshy, M.A. Elbestawi, Additive texturing of metallic surfaces for wetting control, Addit. Manuf. 37 (2021) 101631. https://doi.org/10.1016/j.addma.2020.101631.

[14] M. Može, M. Senegačnik, P. Gregorčič, M. Hočevar, M. Zupančič, I. Golobič, Laser-Engineered Microcavity Surfaces with a Nanoscale Superhydrophobic Coating for Extreme Boiling Performance, ACS Appl. Mater. Interfaces. 12 (2020) 24419–24431. https://doi.org/10.1021/acsami.0c01594.

[15] A. Riveiro, T. Abalde, P. Pou, R. Soto, J. del Val, R. Comesaña, A. Badaoui, M. Boutinguiza, J. Pou, Influence of laser texturing on the wettability of PTFE, Appl. Surf. Sci. 515 (2020). https://doi.org/10.1016/j.apsusc.2020.145984.

[16] R. Pan, H. Zhang, M. Zhong, Triple-Scale Superhydrophobic Surface with Excellent Anti-Icing and Icephobic Performance via Ultrafast Laser Hybrid Fabrication, ACS Appl. Mater. Interfaces. 13 (2021) 1743–1753. https://doi.org/10.1021/acsami.0c16259.

[17] D. Wu, Z. Zhang, Y. Zhang, Y. Jiao, S. Jiang, H. Wu, C. Li, C. Zhang, J. Li, Y. Hu, G. Li, J. Chu, L. Jiang, High-Performance Unidirectional Manipulation of Microdroplets by Horizontal Vibration on Femtosecond Laser-Induced Slant Microwall Arrays, Adv. Mater. 32 (2020) 1–11. https://doi.org/10.1002/adma.202005039.

[18] L. Wang, Z. Tian, G. Jiang, X. Luo, C. Chen, X. Hu, H. Zhang, M. Zhong, Spontaneous dewetting transitions of droplets during icing & melting cycle, Nat. Commun. 13 (2022). https://doi.org/10.1038/s41467-022-28036-x.

[19] G. Yuan, Y. Liu, C.-V. Ngo, C. Guo, Rapid fabrication of anti-corrosion and self-healing superhydrophobic aluminum surfaces through environmentally friendly femtosecond laser processing, Opt. Express. 28 (2020) 35636. https://doi.org/10.1364/oe.400804.

[20] A.Y. Vorobyev, C. Guo, Multifunctional surfaces produced by femtosecond laser pulses, J. Appl. Phys. 117 (2015). https://doi.org/10.1063/1.4905616.

[21] Z. Zhan, M. Elkabbash, J.L. Cheng, J. Zhang, S. Singh, C. Guo, Highly Floatable Superhydrophobic Metallic Assembly for Aquatic Applications, ACS Appl. Mater. Interfaces. 11 (2019) 48512–48517. https://doi.org/10.1021/acsami.9b15540.

[22] Y. Hu, J. Li, J. Tian, Y. Xuan, B. Deng, K.L. McNear, D.G. Lim, Y. Chen, C. Yang, G.J. Cheng, Parallel Nanoshaping of Brittle Semiconductor Nanowires for Strained Electronics, Nano Lett. 16 (2016) 7536–7544. https://doi.org/10.1021/acs.nanolett.6b03366.

[23] Y. Hu, P. Kumar, R. Xu, K. Zhao, G.J. Cheng, Ultrafast direct fabrication of flexible substrate-supported designer plasmonic nanoarrays, Nanoscale. 8 (2016) 172–182. https://doi.org/10.1039/c5nr06899a.

[24] S. Jin, Y. Wang, M. Motlag, S. Gao, J. Xu, Q. Nian, W. Wu, G.J. Cheng, Large-Area Direct Laser-Shock Imprinting of a 3D Biomimic Hierarchical Metal Surface for Triboelectric Nanogenerators, Adv. Mater. 30 (2018) 1–9. https://doi.org/10.1002/adma.201705840.

[25] J. Liu, Y. He, M. Xia, Y. Hu, Utrahigh strain rate-activated superplastic forming of aluminum and gold nanometals, Mater. Des. 221 (2022) 110910. https://doi.org/10.1016/j.matdes.2022.110910.

[26] H. Gao, Y. Hu, Y. Xuan, J. Li, Y. Yang, R. V. Martinez, C. Li, J. Luo, M. Qi, G.J. Cheng, Large-scale nanoshaping of

ultrasmooth 3D crystalline metallic structures, Science (80-.). 346 (2014) 1352–1356. https://doi.org/10.1126/science.1260139.

[27] J. Liu, X. Zhang, Y. He, Z. Zhao, M. Xia, Y. Hu, Suspended water droplet confined laser shock processing at elevated temperatures, Int. J. Mach. Tools Manuf. 179 (2022) 1–20. https://doi.org/10.1016/j.ijmachtools.2022.103917.

[28] Y. Okamoto, T. Okubo, A. Kajitani, A. Okada, High-quality micro-shape fabrication of monocrystalline diamond by nanosecond pulsed laser and acid cleaning, Int. J. Extrem. Manuf. 4 (2022). https://doi.org/10.1088/2631-7990/ac5a6a.

[29] J. Song, D. Wang, L. Hu, X. Huang, Y. Chen, Superhydrophobic surface fabricated by nanosecond laser and perhydropolysilazane, Appl. Surf. Sci. 455 (2018) 771–779. https://doi.org/10.1016/j.apsusc.2018.05.227.

[30] L.B. Boinovich, E.B. Modin, A.R. Sayfutdinova, K.A. Emelyanenko, A.L. Vasiliev, A.M. Emelyanenko, Combination of Functional Nanoengineering and Nanosecond Laser Texturing for Design of Superhydrophobic Aluminum Alloy with Exceptional Mechanical and Chemical Properties, ACS Nano. 11 (2017) 10113–10123. https://doi.org/10.1021/acsnano.7b04634.

[31] A. Samanta, Q. Wang, S.K. Shaw, H. Ding, Nanostructuring of laser textured surface to achieve superhydrophobicity on engineering metal surface, J. Laser Appl. 31 (2019) 022515. https://doi.org/10.2351/1.5096148.

[32] X. Liu, K. Wu, G. Wu, Y. Gao, L. Zhu, Y. Lu, J. Lu, High strength and high ductility copper obtained by topologically controlled planar heterogeneous structures, Scr. Mater. 124 (2016) 103–107. https://doi.org/10.1016/j.scriptamat.2016.07.003.

[33] G. Chen, X. Quan, P. Cheng, Effects of pulse width and mass flux on microscale flow boiling under pulse heating, Int. Commun. Heat Mass Transf. 37 (2010) 792–795. https://doi.org/10.1016/j.icheatmasstransfer.2010.03.007.

[34] Y. Nakata, N. Miyanaga, T. Okada, Effect of pulse width and fluence of femtosecond laser on the size of nanobump array, Appl. Surf. Sci. 253 (2007) 6555–6557. https://doi.org/10.1016/j.apsusc.2007.01.080.

[35] N.P. Kryuchkov, S.O. Yurchenko, Y.D. Fomin, E.N. Tsiok, V.N. Ryzhov, Complex crystalline structures in a two-dimensional core-softened system, Soft Matter. 14 (2018) 2152–2162. https://doi.org/10.1039/c7sm02429k.

[36] K.W. Jacobsen, J.K. Norskov, M.J. Puska, Interatomic interactions in the effective-medium theory, Phys. Rev. B. 35 (1987) 7423–7442. https://doi.org/10.1103/PhysRevB.35.7423.

[37] A. Stukowski, Structure identification methods for atomistic simulations of crystalline materials, Model. Simul. Mater. Sci. Eng. 20 (2012). https://doi.org/10.1088/0965-0393/20/4/045021.

[38] C. Wang, X. Wang, Y. Xu, Z. Gao, Numerical modeling of the confined laser shock peening of the OFHC copper, Int. J. Mech. Sci. 108–109 (2016) 104–114. https://doi.org/10.1016/j.ijmecsci.2016.02.002.

[39] T.P. Remington, B.A. Remington, E.N. Hahn, M.A. Meyers, Deformation and failure in extreme regimes by high-energy pulsed lasers: A review, Mater. Sci. Eng. A. 688 (2017) 429–458. https://doi.org/10.1016/j.msea.2017.01.114.

[40] L. Zhou, Y. Li, W. He, G. He, X. Nie, D. Chen, Z. Lai, Z. An, Deforming TC6 titanium alloys at ultrahigh strain rates during multiple laser shock peening, Mater. Sci. Eng. A. 578 (2013) 181–186. https://doi.org/10.1016/j.msea.2013.04.070.

[41] Y. Mei, J. Zhou, Y. Hao, X. Hu, J. Lin, Y. Huang, L. Li, C. Feng, F. Wu, R. Chen, High-Lithiophilicity Host with Micro/Nanostructured Active Sites based on Wenzel Wetting Model for Dendrite-Free Lithium Metal Anodes, Adv. Funct. Mater. 31 (2021). https://doi.org/10.1002/adfm.202106676.

[42] X. Dai, B.B. Stogin, S. Yang, T.S. Wong, Slippery Wenzel State, ACS Nano. 9 (2015) 9260–9267. https://doi.org/10.1021/acsnano.5b04151.

[43] T.H. Fang, W.L. Li, N.R. Tao, K. Lu, Tensile Plasticity in Gradient, Science (80-.). 331 (2011) 1587–1590.

[44] Y. Wang, F. Guo, Q. He, L. Song, M. Wang, A. Huang, Y. Li, C. Huang, Synergetic deformation-induced extraordinary softening and hardening in gradient copper, Mater. Sci. Eng. A. 752 (2019) 217–222.

https://doi.org/10.1016/j.msea.2019.03.020.

[45] M.N. Hasan, Y.F. Liu, X.H. An, J. Gu, M. Song, Y. Cao, Y.S. Li, Y.T. Zhu, X.Z. Liao, Simultaneously enhancing strength and ductility of a high-entropy alloy via gradient hierarchical microstructures, Int. J. Plast. 123 (2019) 178–195. https://doi.org/10.1016/j.ijplas.2019.07.017.

[46] X. Wu, Y. Zhu, Heterogeneous materials: a new class of materials with unprecedented mechanical properties, Mater. Res. Lett. 5 (2017) 527–532. https://doi.org/10.1080/21663831.2017.1343208.

[47] X. Pan, L. Zhou, C. Wang, K. Yu, Y. Zhu, M. Yi, L. Wang, S. Wen, W. He, X. Liang, Microstructure and residual stress modulation of 7075 aluminum alloy for improving fatigue performance by laser shock peening, Int. J. Mach. Tools Manuf. 184 (2023) 103979. https://doi.org/10.1016/j.ijmachtools.2022.103979.

[48] Z.C. Cordero, B.E. Knight, C.A. Schuh, Six decades of the Hall–Petch effect – a survey of grain-size strengthening studies on pure metals, Int. Mater. Rev. 61 (2016) 495–512. https://doi.org/10.1080/09506608.2016.1191808.

[49] Y.B. Wang, X.Z. Liao, Y.H. Zhao, E.J. Lavernia, S.P. Ringer, Z. Horita, T.G. Langdon, Y.T. Zhu, The role of stacking faults and twin boundaries in grain refinement of a Cu-Zn alloy processed by high-pressure torsion, Mater. Sci. Eng. A. 527 (2010) 4959–4966. https://doi.org/10.1016/j.msea.2010.04.036.

[50] P. Fu, R. Chu, Z. Xu, G. Ding, C. Jiang, Relation of hardness with FWHM and residual stress of GCr15 steel after shot peening, Appl. Surf. Sci. 431 (2018) 165–169. https://doi.org/10.1016/j.apsusc.2017.09.136.

[51] T.Y. Tsui, W.C. Oliver, G.M. Pharr, Influences of stress on the measurement of mechanical properties using nanoindentation: Part I. Experimental studies in an aluminum alloy, J. Mater. Res. 11 (1996) 752–759. https://doi.org/10.1557/JMR.1996.0091.